Research
A SCIENCE PARTNER JOURNAL

RESEARCH ARTICLE

Revealing Majorana Zero Modes in Vortex Cores via Nonmagnetic Impurities

Vyacheslav D. Neverov[1,2,3], Tairzhan Karabassov[1,2], Andrey V. Krasavin[2,3*], Dimitri Roditchev[4], Vasily S. Stolyarov[1,4], and Alexei Vagov[2]

[1]Moscow Institute of Physics and Technology, Dolgoprudny 141700, Russian Federation. [2]HSE University, Moscow 101000, Russian Federation. [3]National Research Nuclear University MEPhI, Moscow 115409, Russian Federation. [4]LPEM, UMR-8213, ESPCI Paris, PSL, CNRS, Sorbonne University, 75005 Paris, France.

*Address correspondence to: avkrasavin@gmail.com

Citation: Neverov VD, Karabassov T, Krasavin AV, Roditchev D, Stolyarov VS, Vagov A. Revealing Majorana Zero Modes in Vortex Cores via Nonmagnetic Impurities. *Research* 2026;9:Article 1087. https://doi.org/10.34133/research.1087

Submitted 13 September 2025
Revised 18 December 2025
Accepted 19 December 2025
Published 23 January 2026

Majorana zero modes (MZMs) localized in vortex cores of topological superconductors are widely regarded promising building blocks for fault-tolerant quantum computation. However, their unambiguous detection is hindered by the extremely small energy spacing separating them from conventional Caroli-de Gennes-Matricon states. Using a microscopic Bogoliubov-de Gennes approach, we demonstrate that nonmagnetic impurities, rather than suppressing, can substantially enhance the energy gap between MZMs and other vortex core excitations. The robustness of MZMs against local perturbations ensures that while conventional states are shifted by impurity-induced potentials, the MZMs remain intact. This results in a pronounced zero-bias peak in the local density of states. Our results dispute the widespread assumption that large Δ / E_F values—where Δ is the superconducting gap and E_F is the Fermi energy—are required to detect MZMs, and instead indicate that purposefully engineered pinning centers in conventional *s*-wave superconductors offer a practical and experimentally accessible alternative.

Introduction

Majorana zero modes (MZMs), first predicted to exist in vortex cores of a *p*-wave superconductor [1], exhibit several exceptional characteristics that have attracted considerable interest from the broader physics community. MZMs, which can be regarded as "half-fermion" excitations, correspond to 2 degenerate states with energies lying exactly at the midpoint of the superconducting gap. These states are localized, yet exhibit nonlocal behavior: in systems containing a single vortex, the MZM wave functions are distributed between the vortex core and the boundary of the sample [2]. MZMs are topologically protected and separated from nearby states by an energy gap, making them robust against local perturbations and low-energy excitations [3]. They are also predicted to appear at the ends of one-dimensional *p*-wave superconducting wires [4]. Their robustness makes them promising candidates for realizing stable qubits in quantum computation architectures [5–7].

Only a few materials are considered potential *p*-wave superconductors, including Sr_2RuO_4 [8], UPt_3 [9], layered $AuSn_4$ [10], and $Cu_xBi_2Se_3$ [11]. However, MZMs can also emerge via the proximity effect at interfaces between conventional *s*-wave superconductors and topological insulators [12], or between *s*-wave superconductors and materials exhibiting ferromagnetic Rashba spin-orbit coupling (SOC) [13]. These mechanisms greatly expand the range of materials and hybrid structures in which MZMs can be realized, sparking an intensive search for their experimental detection [2,14,15].

Signatures of MZMs have been reported in various superconducting devices [16–23] and in complicated scanning tunneling microscopy (STM) studies of certain novel materials [24]. However, the experimental observables used to identify MZMs can also arise from nontopological bound states, making unambiguous identification challenging [25,26]. This ambiguity persists even in the recently presented Majorana 1 quantum processor [7]. Zero-bias peaks in the local density of states (LDOS) observed near vortex cores in iron-based superconductors [27–29] have also been attributed to MZMs. However, such peaks may also originate from alternative quasiparticle excitations, such as Caroli-de Gennes-Matricon (CdGM) states [30–33].

One of the major challenges in observing MZMs is the close proximity of neighboring energy levels. In uniform superconductors, the energies of vortex core excitations are given by [1,30]

$$E_j = \pm j\Delta^2 / E_F, \quad (1)$$

where Δ is the superconducting gap, E_F is the Fermi energy, and j is a quantum number–integer valued for *p*-wave pairing and half-integer for *s*-wave pairing. The MZM corresponds to $j = 0$, representing the only doubly degenerate state in the spectrum. It is separated from the nearest excited states by an energy $\Delta E = \Delta^2 / E_F$. Since $\Delta \ll E_F$ in most superconductors, this energy is extremely small [34], which poses a major obstacle to the experimental resolution and unambiguous detection of MZMs.

To overcome this problem, researchers have turned to materials with small E_F and large Δ [35]. Among these, iron-based superconductors have emerged as leading candidates for MZM observation [27–29,36–48]. However, a serious drawback of iron-based materials is the presence of magnetic impurities from interstitial iron atoms. These impurities suppress the superconducting gap and distort zero-bias peaks, complicating the identification of MZMs [49]. Thus, high-purity single crystals with minimal disorder are essential for reliable conclusions. Furthermore, statistical analysis of bound-state spectra [50] and refined spectroscopy protocols [51] have become crucial tools.

In contrast, nonmagnetic impurities do not affect MZMs due to their topological protection and nonlocal character [1,52]. This distinguishes MZMs from other vortex core states [53,54], offering a possible route for their identification. However, theoretical studies of vortex core states in the presence of pinning centers have shown that while the MZMs remain unperturbed, the energies of other states shift closer together, reducing the visibility of the MZM peak in the LDOS [55]. These results align with the intuitive expectation that disorder leads to spectral crowding and suppression of the visibility of individual states. Nevertheless, experiments on topological superconducting hybrids such as Pb/Co/Si have revealed unexpectedly robust zero-bias peaks, attributed to MZMs, that are separated from other excitations by sizable gaps, presumably arising from magnetic or spin-orbit-induced vortex core textures [56].

This work demonstrates that, contrary to prevailing assumptions and earlier calculations, the mere presence of impurity-induced pinning centers can substantially increase the energy separation between MZMs and other vortex core states, thereby facilitating the identification of the former. With an appropriately chosen impurity potential, in terms of both strength and spatial extent, this energy separation can be substantially enhanced.

Figure 1 illustrates this effect. The top panels (A to D) present results for a clean system: Panel (A) shows the superconducting gap profile within a vortex; panels (B) and (C) display the spatial distribution of the lowest quasiparticle state in trivial and topological superconductors, respectively; and panel (D) depicts the energy dependence of the LDOS. The bottom panels (E to H) show the corresponding results for a system with a pinning potential [indicated by the red line in panel (E)].

These findings suggest that the detection of MZMs becomes considerably more feasible in systems with engineered pinning centers, shifting the focus from materials with high Δ / E_F ratios to more experimentally accessible samples with strategically pinned vortices. Our results are applicable to both intrinsic p-wave superconductors and hybrid structures composed of s-wave superconductors coupled to materials with strong SOC.

Results

The distinction between the MZM and the lowest energy CdGM states in a pure superconductor is illustrated in Fig. 1B and C, which show the spatial density of their respective wave functions. The CdGM state is tightly localized around the vortex core (Fig. 1B). In contrast, the MZM exhibits a nonlocal character, being localized both at the vortex core and near the sample boundary (Fig. 1C). It is worth noting

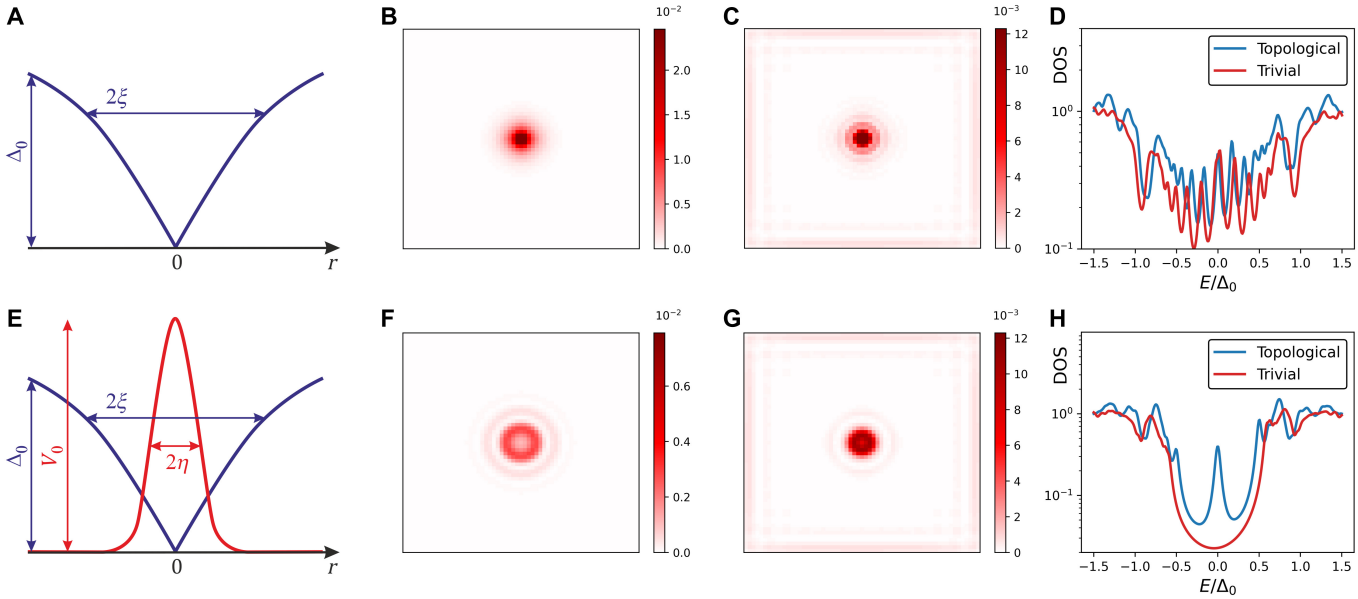

Fig. 1. Top panels: Clean system. (A) Illustration of the geometry and parameters of the system. The blue line shows the vortex core solution for the gap function $|\Delta|$, with characteristic width ξ and homogeneous gap magnitude Δ_0. (B) Spatial profile of the absolute value of the wave function corresponding to the lowest-energy CdGM state in a nontopological superconductor, $V_z = 0$. (C) Spatial profile of the absolute value of the wave function corresponding to the MZM in a topological superconductor with $V_z = 0.5$. (D) Averaged LDOS at the vortex core for topological (blue) and trivial (red) superconductors. Bottom panels: System with pinning potential. (E) Illustration of the geometry and parameters of the system. The red line represents the pinning potential, characterized by its strength V_0 and width η. The blue line shows the vortex core solution for the gap function $|\Delta|$, with characteristic width ξ and homogeneous gap magnitude Δ_0. (F) Spatial profile of the absolute value of the wave function corresponding to the lowest-energy CdGM state in a nontopological superconductor, $V_z = 0$. (G) Spatial profile of the absolute value of the wave function corresponding to the MZM in a topological superconductor with $V_z = 0.5$. (H) Averaged LDOS at the vortex core for topological (blue) and trivial (red) superconductors, shown for $V_0 = 0.8$. The impurity width is set equal to the superconducting coherence length, $\eta = \xi = 3$. The system size is 61×61. In panels (B), (C), (F), and (H), the color bars illustrate the respective distribution density of the wave function for the lower-energy bound state.

that when the system contains 2 or more vortices, the MZM can be distributed or "split" between different vortex cores.

To get a deeper insight, we characterize both the energy and spatial distribution of the quasiparticle states. We calculate the LDOS using

$$N(\mathbf{r},E)=\sum_{n,\sigma}\left|u_{\sigma}^{(n)}(\mathbf{r})\right|^{2}\delta\left(E-E^{(n)}\right)+\left|v_{\sigma}^{(n)}(\mathbf{r})\right|^{2}\delta\left(E+E^{(n)}\right), \quad (2)$$

where the result is smoothed by convoluting with a Lorentzian function of width $\Gamma = 0.01$.

Without the impurity, the averaged LDOS $N(r \leq \xi, E)$ at the vortex core, shown in Fig. 1D of the topological (blue line) and conventional (red line) superconductors, are practically indistinguishable. (In this regard, we note that SOC shifts the energies of the CdGM states, breaking their symmetry around the gap center $E = 0$ [57,58].) However, introducing an impurity substantially modifies the spatial profile of the lowest CdGM state (Fig. 1F) while only slightly perturbing the MZM state (Fig. 1G). This leads to a clear separation of the zero-bias MZM peak at $E = 0$ from the other vortex core states, as clearly evidenced in Fig. 1H.

This impurity-induced restructuring of the LDOS $N(r, E)$ is further explored by examining its spatial dependence on the distance from the impurity r and shown in Fig. 2. The top and bottom panels correspond to the nontopological (A) and topological (B) superconductors, respectively. The results are presented for different values of the pinning potential: $V_0 = 0$ (no pinning), $V_0 = 0.4$, and $V_0 = 0.8$.

Clearly, the states localized at the vortex core exhibit radial symmetry. The radius of the localization ring for these states increases with energy E. In the case of a topological superconductor, the MZM energy is precisely in the middle of the gap, $E = 0$. However, without pinning ($V_0 = 0$), the gap between neighboring excitations is so small that it becomes difficult to distinguish the topological (Fig. 2B) from the nontopological (Fig. 2A) superconductor.

The situation changes when an impurity is introduced into the system. Its potential raises the absolute value of the energies of all the vortex core states, except for the MZM. Consequently, the impurity enhances the energy gap between the MZM and other vortex core states.

The dependence of the energy levels of all vortex states on the impurity potential strength V_0 is shown in Fig. 3. Except for the MZM, the energies of all states in both the topological (Fig. 3A) and nontopological (Fig. 3B) superconductors shift away from the center of the superconducting gap at $E = 0$. Figure 3C illustrates how the energy gap ΔE, which separates the MZM from the other vortex states, varies with V_0. Although this dependence changes with the width η of the impurity potential, it remains monotonic.

We note in passing that the spatial profile of the MZM wave functions differs qualitatively from that of the lowest energy CdGM state—the radial dependence of the MZM wave function exhibits pronounced oscillations (Fig. 4). These oscillations are also visible as scars in the density plot shown in Fig. 1C. Both the period and the amplitude of these oscillations are notably dependent on the impurity strength V_0.

We emphasize that our calculations predict an increase in the energy spacing ΔE for systems with electron-type charge

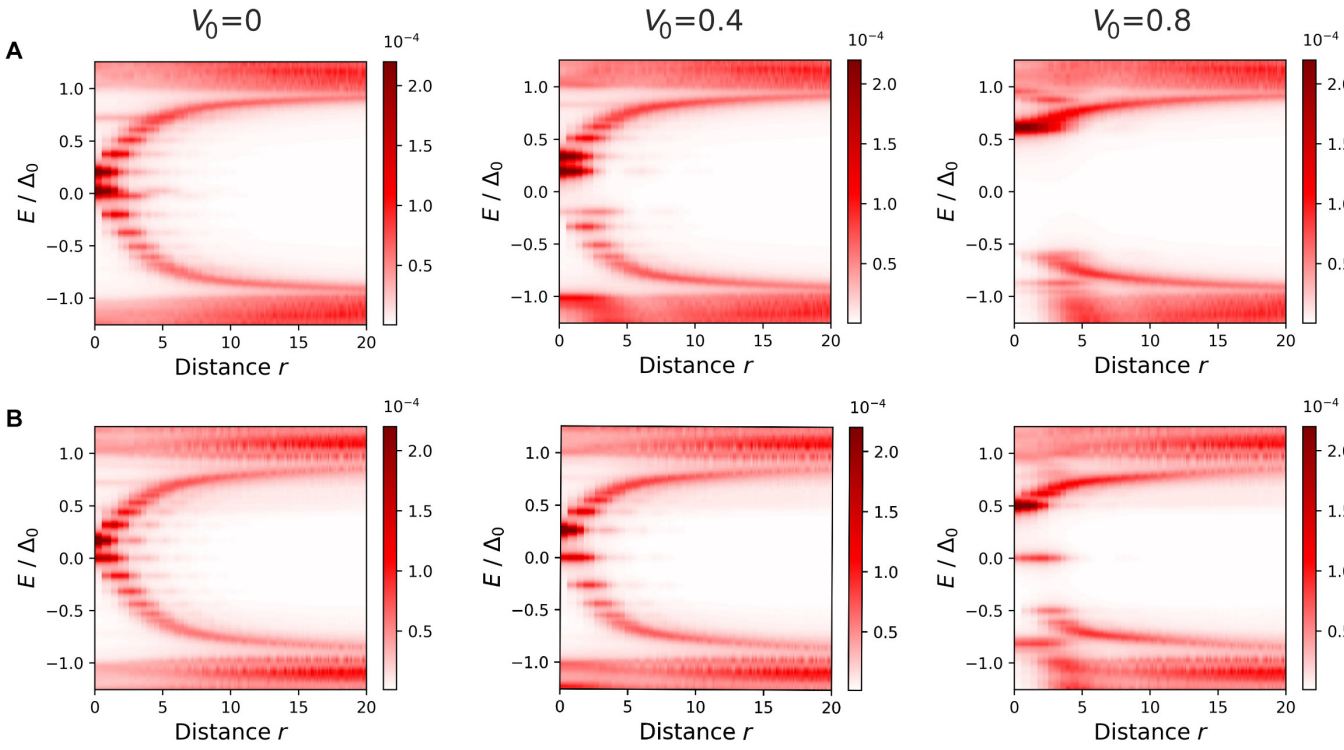

Fig. 2. (A) LDOS for vortex core states in a nontopological (trivial) superconductor ($V_z = 0$), calculated without impurity potential ($V_0 = 0$) and with impurities of strengths $V_0 = 0.4$ and 0.8. (B) LDOS for vortex core states in a topological superconductor ($V_z = 0.5$), calculated without impurity potential ($V_0 = 0$) and with impurities of strengths $V_0 = 0.4$ and 0.8. The impurity width is set equal to the superconducting coherence length, $\eta = \xi = 3$. The color bars are adjusted to the maximum value across all the parameter sets considered.

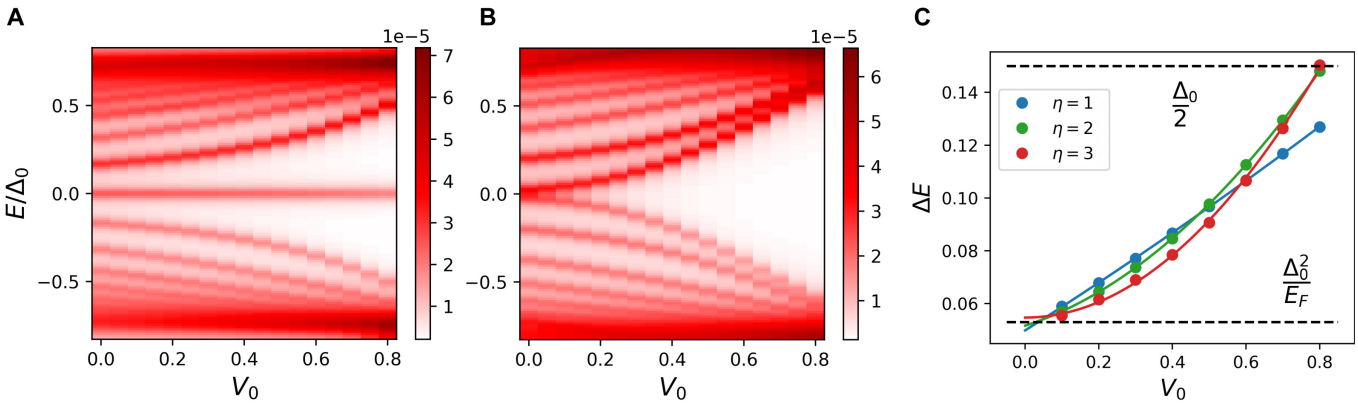

Fig. 3. Dependence of the energy levels of the vortex core states on the impurity potential strength V_0 for the topological (A) and nontopological (B) superconductors. The calculations assume that the impurity width is equal to the superconducting coherence length, $\eta = \xi = 3$. The color bars indicate the value of DOS. (C) The variation of the energy gap ΔE between the MZM and other vortex core states as a function of pinning strength V_0, computed for impurity widths $\eta = 1, 2$, and 3. The lines between points are shown as guides to the eye.

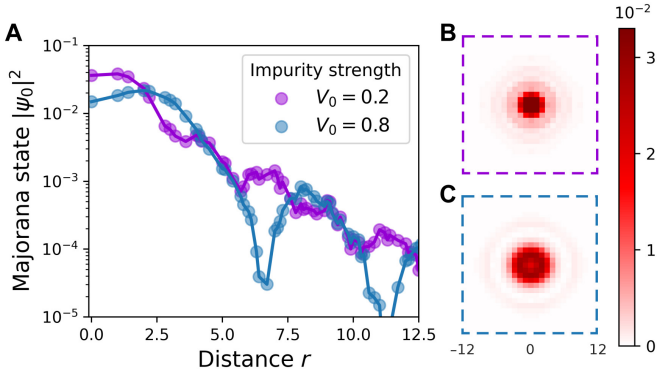

Fig. 4. (A) Radial dependence of the MZM wave function as a function of distance r from the vortex core, calculated for impurity strengths $V_0 = 0.2$ and 0.8. Panels (B) and (C) show density plots of the spatial distribution of the MZM wave function for $V_0 = 0.2$ and 0.8, respectively. The impurity width is set equal to the superconducting coherence length, $\eta = \xi = 3$. The color bar is normalized to the maximum value of the density of the wave function for both panels.

carriers, which occurs when the chemical potential is negative, $\mu < 0$ ($\mu = 0$ corresponds to the center of the conduction band). In contrast, for systems with hole-type carriers ($\mu > 0$), the impurity potential has the opposite effect: it shifts the energies of the vortex core states toward the center of the superconducting gap, $E = 0$. This reversed behavior was previously reported in Ref. [55], where it was concluded that impurities may further suppress the visibility of MZMs. A similar effect is observed when the impurity potential becomes attractive for electrons ($V_0 < 0$), again leading to a shift of the vortex core states toward $E = 0$.

At first glance, these findings suggest that the outcome strongly depends on the impurity type and the nature of the charge carriers. However, this interpretation is misleading. Calculations predicting the reverse effect also rely on the same approximation (Eq. 9), which becomes invalid when the impurity attracts quasiparticles ($V_0 < 0$) or the system becomes hole-like ($\mu > 0$). In such cases, the vortex is repelled by the impurity, rendering the solution based on Eq. 9 unstable. Therefore, adding "usual" impurities $V_0 > 0$ can only enhance the visibility of MZMs, not suppress it, as in this case the vortex is strongly pinned to the impurity, which effectively acts as a local potential barrier that pushes the higher-energy CdGM states away from MZM.

Conclusion

In this work, we have investigated the effect of an impurity potential on MZMs localized in the vortex core of a hybrid topological superconductor, composed of a conventional *s*-wave superconductor, a Rashba spin-orbit coupled semiconductor, and a ferromagnetic material.

Our direct numerical calculations based on a microscopic model show that introducing nonmagnetic impurities increases the energy separation between MZMs and other vortex core states, while the MZMs themselves remain robust. This finding substantially relaxes the conventional requirement for a high Δ / E_F ratio, which has traditionally hindered the experimental detection of MZMs due to the typically small energy spacing between MZMs and low-energy in-gap excitations. Our results suggest that, rather than relying on materials with large Δ / E_F ratios (such as iron-based superconductors), it is feasible to observe MZMs in hybrid topological systems based on conventional *s*-wave superconductors containing single, strategically engineered nonmagnetic impurities.

Results of the work remain valid as long as the width of the impurity lies within the range $1 / k_F \lesssim \eta \lesssim \xi$, ensuring that it does not exceed the size of the vortex core and V_0 is high enough to suppress superconducting gap.

Our 2-dimensional model captures the essential surface physics governing topological superconductivity and MZM formation in relevant 3-dimensional (3D) platforms. It is directly applicable to 3D samples with columnar defects, where MZMs remain localized at the vortex ends. Surface defects, such as those created by focused nanoscale ion beams or arising from band bending [49,59,60], are likewise expected to yield a comparable widening of the minigap in the surface LDOS, owing to the suppressed contribution from relevant bulk states near the surface.

We finally note that strongly pinned vortices are not ideal for direct motion-based braiding schemes proposed for quantum computations; nevertheless, MZM states at such vortices can still be controlled via alternative approaches. For instance, manipulation can be achieved by controlling the MZM's entangled partner at the sample boundary. This strategy enables

control of MZM's via local gating or phase biasing without moving the vortices themselves [61]. In this context, the proposed mechanism for reliable MZM detection in readily available materials could be essential for designing MZM-based quantum computation schemes.

Methods

The model of topological superconductor

We consider a hybrid topological superconductor that comprises layers of a superconductor with *s*-wave pairing symmetry, a semiconductor with Rashba SOC, and a ferromagnetic insulator. Such a system is described using the discrete model Hamiltonian [62]

$$H = H_s + H_{\mathrm{SOC}} + H_m, \tag{3}$$

where the Hamiltonian of the superconducting subsystem is written in the mean-field approximation as

$$H_s = \sum_{\langle i,j\rangle,\sigma} t_{ij} c^{\dagger}_{i\sigma} c_{j\sigma} + \sum_i \left(\Delta_i c^{\dagger}_{i\uparrow} c^{\dagger}_{i\downarrow} + h.c. \right), \tag{4}$$

with $c_{i\sigma}$ being the electron operators corresponding to lattice site i and spin σ. The hopping elements $t_{ij} = t$ are nonzero only for nearest neighbors, and Δ_i is the gap function at site i. The magnetic part is described by the Hamiltonian

$$H_m = V_z \sum_i \left(c^{\dagger}_{i\uparrow} c_{i\uparrow} - c^{\dagger}_{i\downarrow} c_{i\downarrow} \right), \tag{5}$$

with V_z characterizing the Zeeman splitting. Finally, the Rashba interaction Hamiltonian is given by

$$\begin{aligned} H_{\mathrm{SOC}} = \frac{\alpha}{2} \sum_i \Big[& \left(c^{\dagger}_{i-e_x\downarrow} c_{i\uparrow} - c^{\dagger}_{i+e_x\downarrow} c_{i\uparrow} \right) + \\ & i \left(c^{\dagger}_{i-e_y\downarrow} c_{i\uparrow} - c^{\dagger}_{i+e_y\downarrow} c_{i\uparrow} \right) + h.c. \Big], \end{aligned} \tag{6}$$

where α is the SOC hopping amplitude responsible for spin-flip hopping between nearest neighbors.

We also consider an additional contribution due to an impurity located at position $\mathbf{r}_0$, described by a Gaussian potential

$$V_i = V_0 \exp\left(-\frac{|\mathbf{r}_i - \mathbf{r}_0|^2}{2\eta^2} \right), \tag{7}$$

where V_0 denotes the strength of the impurity and η its spatial extent. Compared to the Fu–Kane model, the Hamiltonian (Eq. 3) includes extra kinetic and Zeeman terms, allowing a trivial phase.

The vortex core states are studied by solving the Bogoliubov-de Gennes (BdG) equations corresponding to the model Hamiltonian (Eq. 3). The approach follows the methodology used for the analysis of CdGM states in conventional *s*-wave superconductors [61–65]. In block-matrix form, the BdG equations are written as

$$\begin{bmatrix} \hat{h}_+ & \hat{g} & 0 & \hat{\Delta} \\ -\hat{g} & \hat{h}_- & \hat{\Delta} & 0 \\ 0 & \hat{\Delta}^* & -\hat{h}^*_+ & -\hat{g}^* \\ \hat{\Delta}^* & 0 & \hat{g}^* & -\hat{h}^*_- \end{bmatrix} \begin{pmatrix} \vec{u}_+ \\ \vec{u}_- \\ \vec{v}_+ \\ \vec{v}_- \end{pmatrix} = E \begin{pmatrix} \vec{u}_+ \\ \vec{u}_- \\ \vec{v}_+ \\ \vec{v}_- \end{pmatrix}, \tag{8}$$

where the components of the eigenvectors $\vec{u}_\sigma$ and $\vec{v}_\sigma$ correspond to lattice sites i. The elements of the block matrices are defined as $\left[\hat{h}\pm\right]_{ij} = t_{ij} + \left(V_i \pm V_z - \mu\right)\delta_{ij}$, with δ_{ij} being the Kronecker delta; $\left[\hat{g}\right]_{ij} = \alpha_{ij}$, where α_{ij} takes values of $\pm\,\alpha/2$ for right/left neighbors and $\pm\, i\alpha/2$ for upper/lower neighbors; and $[\Delta]_{ij} = \Delta_i \delta_{ij}$.

Details of calculations

To obtain the vortex solution, Eq. 8 must be solved in the presence of a magnetic field, which is incorporated by introducing the Peierls phase factor into the hopping integrals as $t_{ij}\exp\left(i \int_{\mathbf{r}_i}^{\mathbf{r}_j} \mathbf{A}(\mathbf{r}) d\mathbf{r}/\phi_0 \right)$, where $\mathbf{A}(\mathbf{r})$ is the vector potential of the magnetic field and ϕ_0 is the flux quantum. The solution for the vortex must satisfy the self-consistency conditions for Δ_i as well as for the field $\mathbf{A}$. Achieving full self-consistency in the presence of the magnetic field requires 2 iterative cycles [63].

Solving the BdG equations exactly is computationally demanding. To reduce the computational load, we employ a simplified approach in which the vortex solution is approximated as follows:

$$\Delta_i = \Delta_0 e^{i\theta_i} \tanh\left(\frac{|\,\mathbf{r}_i - \mathbf{r}_0\,|}{\xi} \right), \tag{9}$$

where Δ_0 represents the homogeneous gap magnitude, $|\,\mathbf{r}_i - \mathbf{r}_0\,|$ is the distance from the vortex center, ξ denotes the coherence length, and θ_i is the polar angle at the lattice site i. Comparison with the exact self-consistent solution shows that this approximation is highly accurate when the superconductor is well within the type II regime [63,66]. Another necessary condition is that the impurity potential is weak, satisfying $V_0 \ll W$, where $W = 8t$ is the bandwidth, and that $\eta \lesssim \xi$. However, we employ the exact self-consistent solution to confirm whether the vortex is attracted to the impurity, acting as a pinning center, or repelled by it. We also note that a solution of the BdG equations depends on the system temperature ($T = 0$ in our calculations), which enters Eq. 9 via temperature-dependent quantities Δ_0 and ξ.

Numerical calculations are performed on a finite sample of size 61×61 (measured in units of the lattice constant a), with boundary conditions set as $u = v = 0$. All energy values are expressed in units of the hopping constant, with $t = 1$ serving as the energy scale. We set the SOC constant to $\alpha = 1.2$ in accordance with Ref. [61], which demonstrated the existence of the topological phase at this level of SOC, and the chemical potential to $\mu = -3.5$, which corresponds to a shallow electron-like band.

We also take $\Delta_0 = 0.3$ and $\xi = 3$, which is substantially smaller than the sample size L. The relative values of the chosen parameters are illustrated in Fig. 1E, which plots the profile of the gap function in the vortex core (blue line) and the impurity potential (red line). The choice ensures the applicability of the approximate solution (Eq. 9).

The Zeeman splitting V_z governs the topological nature of the vortex core states. When $V_z = 0$, the system is a trivial superconductor featuring CdGM states localized around the vortex core. However, when Zeeman splitting satisfies the condition $(4t - |\mu|)^2 + \Delta_0^2 < V_z^2 < \mu^2 + \Delta_0^2$, the system becomes a topological superconductor that hosts MZMs near the vortex core [67]. In the present study, we choose $V_z = 0.5$, which falls

within this range, thus placing the system in the topological superconductor regime.

Acknowledgments

Funding: We gratefully acknowledge the financial support from the Ministry of Science and Higher Education of the Russian Federation in the framework of Agreement No. 075-15-2025-608. A.V., A.V.K., and V.D.N. acknowledge the support of the Basic Research Program and the HPC facilities [68] of HSE University, which were utilized for the numerical solution of the BdG equations.
Author contributions: Conceptualization: V.D.N. and A.V.K. Methodology: V.D.N., T.K., D.R., and V.S.S. Data analysis: V.D.N., T.K., A.V.K., and A.V. Writing—original draft: V.D.N., A.V.K., D.R., V.S.S., and A.V. Writing—review and editing: V.D.N., T.K., A.V.K., and A.V. All authors contributed to discussions and commented on the manuscript.
Competing interests: The authors declare that they have no competing interests.

Data Availability

All data needed to evaluate the conclusions in the paper are freely available at https://gitlab.com/center-quantum-metamaterials/impurity_and_mzm/.

References

1. Volovick GE. Fermion zero modes on vortices in chiral superconductors. *JETP Lett*. 1999;70(9):609–614.
2. Alicea J. New directions in the pursuit of majorana fermions in solid state systems. *Rep Prog Phys*. 2012;75(7):Article 076501.
3. Lahtinen V, Pachos J. A short introduction to topological quantum computation. *SciPost Phys*. 2017;3(3):Article 021.
4. Kitaev AY. Unpaired majorana fermions in quantum wires. *Physics-Uspekhi*. 2001;44(10S):131.
5. Nayak C, Simon SH, Stern A, Freedman M, Sarma SD. Non-abelian anyons and topological quantum computation. *Rev Mod Phys*. 2008;80(3):1083–1159.
6. Sarma SD, Freedman M, Nayak C. Majorana zero modes and topological quantum computation. *npj Quant Inf*. 2015;1(1):15001.
7. Microsoft Azure Quantum, Aghaee M, Alcaraz Ramirez A, Alam Z, Ali R, Andrzejczuk M, Antipov A, Astafev M, Barzegar A, Bauer B, et al. Interferometric single-shot parity measurement in InAs–Al hybrid devices. *Nature*. 2025;638(8051):651–655.
8. Mackenzie AP, Maeno Y. The superconductivity of Sr_2RuO_4 and the physics of spin-triplet pairing. *Rev Mod Phys*. 2003;75(2):657–712.
9. Joynt R, Taillefer L. The superconducting phases of UPt_3. *Rev Mod Phys*. 2002;74(1):235–294.
10. Zhu W, Song R, Huang J, Wang Q-W, Cao Y, Zhai R, Bian Q, Shao Z, Jing H, Zhu L, et al. Intrinsic surface p-wave superconductivity in layered AuSn4. *Nat Commun*. 2023;14(1):Article 7012.
11. Sasaki S, Kriener M, Segawa K, Yada K, Tanaka Y, Sato M, Ando Y. Topological superconductivity in $Cu_xBi_2Se_3$. *Phys Rev Lett*. 2011;107(21):Article 217001.
12. Liang F, Kane CL. Superconducting proximity effect and majorana fermions at the surface of a topological insulator. *Phys Rev Lett*. 2008;100(9):Article 096407.
13. Sau JD, Lutchyn RM, Tewari S, Das Sarma S. Generic new platform for topological quantum computation using semiconductor heterostructures. *Phys Rev Lett*. 2010;104(4):Article 040502.
14. Flensberg K, von Oppen F, Stern A. Engineered platforms for topological superconductivity and majorana zero modes. *Nat Rev Mater*. 2021;6(10):944–958.
15. Li C, Luo X-J, Chen L, Liu DE, Zhang FC, Liu X. Controllable majorana vortex states in iron-based superconducting nanowires. *Natl Sci Rev*. 2022;9(9):Article nwac095.
16. Rokhinson LP, Liu X, Furdyna JK. The fractional a.c. Josephson effect in a semiconduc tor–superconductor nanowire as a signature of Majorana particles. *Nat Phys*. 2012;8(11):795–799.
17. Deng MT, Yu CL, Huang GY, Larsson M, Caroff P, Xu HQ. Anomalous zero-bias conductance peak in a Nb–InSb nanowire–Nb hybrid device. *Nano Lett*. 2012;12(12):6414–6419.
18. Das A, Ronen Y, Most Y, Oreg Y, Heiblum M, Shtrikman H. Zero-bias peaks and splitting in an Al–InAs nanowire topological super conductor as a signature of Majorana fermions. *Nat Phys*. 2012;8(12):887–895.
19. Churchill HOH, Fatemi V, Grove-Rasmussen K, Deng MT, Caroff P, Xu HQ, Marcus CM. Superconductor-nanowire devices from tunneling to the multichannel regime: Zero-bias oscillations and magneto conductance crossover. *Phys Rev B*. 2013;87(24):Article 241401.
20. Oostinga JB, Maier L, Schüffelgen P, Knott D, Ames C, Brüne C, Tkachov G, Buhmann H, Molenkamp LW. Josephson supercurrent through the topological surface states of strained bulk hgte. *Phys Rev X*. 2013;3(2):Article 021007.
21. Deng MT, Yu CL, Huang GY, Larsson M, Caroff P, Xu HQ. Parity independence of the zero-bias conductance peak in a nanowire based topological superconductor-quantum dot hybrid device. *Sci Rep*. 2014;4(1):7261.
22. Wang D-F. Quantum wonderland beneath a microscopic tip: Constructing and probing topological super conductors with atomic precision. *Physics*. 2025;54(5):332–343.
23. Yang G, Lyu Z, Wang J, Ying J, Zhang X, Shen J, Liu G, Fan J, Ji Z, Jing X, et al. Protected gap closing in josephson trijunctions constructed on Bi_2Te_3. *Phys Rev B*. 2019;100(18):Article 180501.
24. Liu T, Wan CY, Yang H, Zhao Y, Xie B, Zheng W, Yi Z, Guan D, Wang S, Zheng H, et al. Signatures of hybridization of multiple majorana zero modes in a vortex. *Nature*. 2024;633(8028):71–76.
25. Lee EJH, Jiang X, Houzet M, Aguado R, Lieber CM, De Franceschi S. Spin-resolved Andreev levels and parity crossings in hybrid superconductor–semiconductor nanostructures. *Nat Nanotechnol*. 2014;9(1):79–84.
26. Deng MT, Vaitiekėnas S, Hansen EB, Danon J, Leijnse M, Flensberg K, Nygård J, Krogstrup P, Marcus CM. Majorana bound state in a coupled quantum-dot hybrid-nanowire system. *Science*. 2016;354(6319):1557–1562.
27. Wang D, Kong L, Fan P, Chen H, Zhu S, Wenyao Liu L, Cao YS, Shixuan D, Schneeloch J, Zhong R, et al. Evidence for majorana bound states in an iron-based superconductor. *Science*. 2018;362(6412):333–335.
28. Zhu S, Kong L, Cao L, Chen H, Papaj M, Du S, Xing Y, Liu W, Wang D, Shen C, et al. Nearly quantized conductance plateau of vortex zero mode in an iron-based superconductor. *Science*. 2020;367(6474):189–192.

29. Kong L, Zhu S, Papaj M, Chen H, Cao L, Isobe H, Xing Y, Liu W, Wang D, Fan P, et al. Half-integer level shift of vortex bound states in an iron-based superconductor. *Nat Phys*. 2019;15(11):1181–1187.
30. Caroli C, De Gennes PG, Matricon J. Bound fermion states on a vortex line in a type II superconductor. *Phys Lett*. 1964;9(4):307–309.
31. Chen M, Chen X, Yang H, Zengyi D, Zhu X, Wang E, Wen H-H. Discrete energy levels of Caroli-de Gennes-Matricon states in quantum limit in $FeTe_{0.55}Se_{0.45}$. *Nat Commun*. 2018;9(1): Article 970.
32. Chen C, Liu Q, Bao WC, Yan Y, Wang QH, Zhang T, Feng D. Observation of discrete conventional Caroli–de Gennes–Matricon states in the vortex core of single-layer FeSe/$SrTio_3$. *Phys Rev Lett*. 2020;124(9):Article 097001.
33. Gozlinski T, Li Q, Heid R, Nemoto R, Willa R, Yamada TK, Schmalian J, Wulfhekel W. Band-resolved Caroli–de Gennes–Matricon states of multiple-flux-quanta vortices in a multiband superconductor. *Sci Adv*. 2023;9(36):Article eadh9163.
34. Stolyarov VS, Roditchev D, Gurtovoi VL, Kozlov SN, Yakovlev DS, Skryabina OV, Vinokur VM, Golubov AA. Resonant oscillations of Josephson current in Nb-Bi2Te2.3Se0.7-Nb junctions. *Adv Quantum Technol*. 2022;5(3). https://doi.org/10.1002/qute.202100124
35. Liu Q, Chen C, Zhang T, Peng R, Yan Y-J, Wen C-H-P, Lou X, Huang Y-L, Tian J-P, Dong X-L, et al. Robust and clean majorana zero mode in the vortex core of high-temperature superconductor $(Li_{0.84}Fe_{0.16})$OHFeSe. *Phys Rev X*. 2018;8(4):Article 041056.
36. Machida T, Hanaguri T. Searching for majorana quasiparticles at vortex cores in iron-based superconductors. *Prog Theor Exp Phys*. 2024;2024(8):Article 08C103.
37. Kong L-Y, Ding H. Emergent vortex majorana zero mode in iron-based superconductors. *Acta Phys Sin*. 2020;69: Article 110301.
38. Li M, Geng Li L, Cao XZ, Wang X, Jin C, Chiu C-K, Pennycook SJ, Wang Z, Gao H-J. Ordered and tunable majorana-zero-mode lattice in naturally strained LiFeAs. *Nature*. 2022;606(7916):890–895.
39. Kong L, Cao L, Zhu S, Papaj M, Dai G, Li G, Fan P, Liu W, Yang F, Wang X, et al. Majorana zero modes in impurity-assisted vortex of LiFeAs super conductor. *Nat Commun*. 2021;12(1):Article 4146.
40. Fan P, Yang F, Qian G, Chen H, Zhang Y-Y, Li G, Huang Z, Xing Y, Kong L, Liu W, et al. Observation of magnetic adatom-induced majorana vortex and its hybridization with field-induced majorana vortex in an iron-based superconductor. *Nat Commun*. 2021;12(1):Article 1348.
41. Ge J-F, Bastiaans KM, Chatzopoulos D, Cho D, Tromp WO, Benschop T, Niu J, Genda G, Allan MP. Single electron charge transfer into putative majorana and trivial modes in individual vortices. *Nat Commun*. 2023;14(1):Article 3341.
42. Lun-Hui H, Zhang R-X. Dislocation majorana bound states in iron-based superconductors. *Nat Commun*. 2024;15(1): Article 2337.
43. Liu W, Cao L, Zhu S, Kong L, Wang G, Papaj M, Zhang P, Liu YB, Chen H, Li G, et al. A new majorana platform in an Fe-As bilayer superconductor. *Nat Commun*. 2020;11(1):Article 5688.
44. Pathak V, Plugge S, Franz M. Majorana bound states in vortex lattices on iron-based superconductors. *Ann Phys*. 2021;435:Article 168431.
45. Li G, Zhu S, Wang D, Wang Y, Gao H-J. Recent progress of scanning tunneling microscopy/spectroscopy study of majorana bound states in the $FeTe_{0.55}Se_{0.45}$ superconductor. *Supercond Sci Technol*. 2021;34(7):Article 073001.
46. Chiu CK, Machida T, Huang Y, Hanaguri T, Zhang FC. Scalable majorana vortex modes in iron-based superconductors. *Sci Adv*. 2020;6(9):Article eaay0443.
47. Zhu Z, Zheng H, Jia JF. Majorana zero mode in the vortex of artificial topological superconductor. *J Appl Phys*. 2021;129(15):Article 151104.
48. Lun-Hui H, Xianxin W, Liu C-X, Zhang R-X. Competing vortex topologies in iron-based superconductors. *Phys Rev Lett*. 2022;129(27):Article 277001.
49. Massee F, Sprau PO, Wang YL, Davis JS, Ghigo G, Gu GD, Kwok WK. Imaging atomic-scale effects of high-energy ion irradiation on superconductivity and vortex pinning in Fe(Se, Te). *Sci Adv*. 2015;1(4):1500033.
50. Machida T, Sun Y, Pyon S, Takeda S, Kohsaka Y, Hanaguri T, Sasagawa T, Tamegai T. Zero energy vortex bound state in the superconducting topological surface state of Fe(Se, Te). *Nat Mater*. 2019;18(8):811–815.
51. Ziesen A, Altland A, Egger R, Hassler F. Statistical Majorana bound state spectroscopy. *Phys Rev Lett*. 2023;130(10): Article 106001.
52. Smith ED, Tanaka K, Nagai Y. Manifestation of chirality in the vortex lattice in a two dimensional topological superconductor. *Phys Rev B*. 2016;94(6):Article 064515.
53. Khodaeva UE, Skvortsov MA. Vortex core near planar defects in a clean layered superconductor. *Phys Rev B*. 2022;105(13):Article 134504.
54. Samokhvalov AV, Plastovets VD, Mel'Nikov AS. Topological transitions in electronic spectra: Crossover between abrikosov and josephson vortices. *Phys Rev B*. 2020;102(17): Article 174501.
55. de Mendonca BS, Manesco ALR, Sandler N, Luis GGV, da Silva D. Near zero energy Caroli–de Gennes–Matricon vortex states in the presence of impurities. *Phys Rev B*. 2023;107(18):Article 184509.
56. Ménard GC, Mesaros A, Brun C, Debontridder F, Roditchev D, Simon P, Cren T. Isolated pairs of Majorana zero modes in a disordered superconducting lead monolayer. *Nat Commun*. 2019;10(1):Article 2587.
57. Cayao J, Prada E, San-Jose P, Aguado R. SNS junctions in nanowires with spin-orbit cou pling: Role of confinement and helicity on the subgap spectrum. *Phys Rev B*. 2015;91(2): Article 024514.
58. Cayao J, Black-Schaffer AM. Distinguishing trivial and topological zero-energy states in long nanowire junctions. *Phys Rev B*. 2021;104(2):Article L020501.
59. Yang H, Li Y-Y, Liu T-T, Xue H-Y, Guan D-D, Wang S-Y, Zheng H, Liu C-H, Liang F, Jia J-F. Superconductivity of topological surface states and strong proximity effect in $Sn_{1-x}Pb_xTe$-Pb heterostructures. *Adv Mater*. 2019;31(52): Article 1905582.
60. Xie B, Yi Z, Zheng W, Gao Z, Guan D, Liu X, Liu L, Wang S, Zheng H, Liu C, et al. Strong superconducting proximity compatible with fermi-level tuning at top surfaces of bulk insulating SnTe-type semiconductors. *Nano Lett*. 2025;25(19):7981–7988.
61. Liang Q-F, Wang Z, Xiao H. Manipulation of Majorana fermions by point-like gate voltage in the vortex state of a topological superconductor. *Europhys Lett*. 2012;99(5):50004.

62. Björnson K, Black-Schaffer AM. Vor tex states and Majorana fermions in spin-orbit coupled semiconductor-superconductor hybrid structures. *Phys Rev B*. 2013;88(2):Article 024501.
63. Neverov VD, Kalashnikov A, Lukyanov AE, Krasavin AV, Croitoru MD, Vagov A. Fully microscopic treatment of magnetic field using Bogoliubov–de Gennes approach. *Condens Matter*. 2024;9(1):8.
64. Fang D. Vortex bound states influenced by the fermi surface anisotropy. *Chin Phys B*. 2023;32(3):Article 037403.
65. Fan X, Chen X, Yang H, Wen H-H. Distinct properties of vortex bound states driven by temperature. *Europhys Lett*. 2021;136(4):46002.
66. Neverov VD, Lukyanov AE, Krasavin AV, Shanenko AA, Croitoru MD, Vagov A. Microscopic description of intermediate mixed state in superconductors between the first and second types. *Phys Rev B*. 2024;110(5): Article 054502.
67. Sato M, Takahashi Y, Fujimoto S. Non-Abelian topological orders and Majorana fermions in spin-singlet superconductors. *Phys Rev B*. 2010;82(13):Article 134521.
68. Kostenetskiy PS, Chulkevich RA, Kozyrev VI. HPC resources of the higher school of economics. *J Phys Conf Ser*. 2021;1740(1):Article 012050.

Research
A SCIENCE PARTNER JOURNAL

Revealing Majorana Zero Modes in Vortex Cores via Nonmagnetic Impurities

Vyacheslav D. Neverov, Tairzhan Karabassov, Andrey V. Krasavin, Dimitri Roditchev, Vasily S. Stolyarov, and Alexei Vagov

Citation: Neverov V, Karabassov T, Krasavin A, Roditchev D, Stolyarov V, Vagov A. Revealing Majorana Zero Modes in Vortex Cores via Nonmagnetic Impurities. *Research*. 2026;**9**:1087. DOI: 10.34133/research.1087

Majorana zero modes (MZMs) localized in vortex cores of topological superconductors are widely regarded promising building blocks for fault-tolerant quantum computation. However, their unambiguous detection is hindered by the extremely small energy spacing separating them from conventional Caroli-de Gennes-Matricon states. Using a microscopic Bogoliubov-de Gennes approach, we demonstrate that nonmagnetic impurities, rather than suppressing, can substantially enhance the energy gap between MZMs and other vortex core excitations. The robustness of MZMs against local perturbations ensures that while conventional states are shifted by impurity-induced potentials, the MZMs remain intact. This results in a pronounced zero-bias peak in the local density of states. Our results dispute the widespread assumption that large #/EF values—where # is the superconducting gap and EF is the Fermi energy—are required to detect MZMs, and instead indicate that purposefully engineered pinning centers in conventional *s*-wave superconductors offer a practical and experimentally accessible alternative.
Image

Research (ISSN 2639-5274) is published by the American Association for the Advancement of Science. 1200 New York Avenue NW, Washington, DC 20005.